PHILOSOPHICAL TRANSACTIONS A

royalsocietypublishing.org/journal/rsta

Research

Cite this article: Brown R *et al*. 2021 Motion estimation and correction for simultaneous PET/MR using SIRF and CIL. *Phil. Trans. R. Soc. A* **379**: 20200208.
https://doi.org/10.1098/rsta.2020.0208

Accepted: 7 April 2021

One contribution of 9 to a theme issue 'Synergistic tomographic image reconstruction: part 2'.

Subject Areas:
medical physics

Keywords:
Motion, correction, estimation, PET, MR, SIRF

Author for correspondence:
Kris Thielemans
e-mail: k.thielemans@ucl.ac.uk

Motion estimation and correction for simultaneous PET/MR using SIRF and CIL

Richard Brown[1,2], Christoph Kolbitsch[2,3], Claire Delplancke[4], Evangelos Papoutsellis[5,6], Johannes Mayer[3], Evgueni Ovtchinnikov[5], Edoardo Pasca[5], Radhouene Neji[2,7], Casper da Costa-Luis[2], Ashley G. Gillman[8], Matthias J. Ehrhardt[4,9], Jamie R. McClelland[10,11], Bjoern Eiben[10,11] and Kris Thielemans[1,11]

[1]Institute of Nuclear Medicine, University College London, London, UK
[2]School of Biomedical Engineering and Imaging Sciences, King's College London, London, UK
[3]Physikalisch-Technische Bundesanstalt, Braunschweig and Berlin, Germany
[4]Department of Mathematical Sciences, University of Bath, Bath, UK
[5]Scientific Computing Department, STFC, UKRI, Rutherford Appleton Laboratory, Harwell Campus, Didcot, UK
[6]Henry Royce Institute, Department of Materials, The University of Manchester, Manchester, UK
[7]MR Research Collaborations, Siemens Healthcare, Frimley, UK
[8]Australian e-Health Research Centre, Commonwealth Scientific and Industrial Research Organisation, Townsville, Australia
[9]Institute for Mathematical Innovation, University of Bath, UK
[10]Centre for Medical Image Computing, University College London, UK
[11]Department of Medical Physics and Biomedical Engineering, University College London, UK

RB, 0000-0001-6989-9200; CK, 0000-0002-4355-8368; CD, 0000-0001-7483-0419; EPap, 0000-0002-1820-9916; JM, 0000-0002-2500-445X; EPas, 0000-0001-6957-2160; CCL, 0000-0002-7211-1557; AGG, 0000-0001-9130-1092; MJE, 0000-0001-8523-353X; JRM, 0000-0002-4922-0093; BE, 0000-0002-5908-251X; KT, 0000-0002-5514-199X

THE ROYAL SOCIETY PUBLISHING

SIRF is a powerful PET/MR image reconstruction research tool for processing data and developing new algorithms. In this research, new developments to SIRF are presented, with focus on motion estimation and correction. SIRF's recent inclusion of the adjoint of the resampling operator allows gradient propagation through resampling, enabling the MCIR technique. Another enhancement enabled registering and resampling of complex images, suitable for MRI. Furthermore, SIRF's integration with the optimization library CIL enables the use of novel algorithms. Finally, SPM is now supported, in addition to NiftyReg, for registration. Results of MR and PET MCIR reconstructions are presented, using FISTA and PDHG, respectively. These demonstrate the advantages of incorporating motion correction and variational and structural priors.

This article is part of the theme issue 'Synergistic tomographic image reconstruction: part 2'.

1. Introduction

Multi-modality imaging has enabled a leap forward in medical imaging. The combination of information obtained from two or more physical processes can provide powerful information for diagnosis, disease staging and/or therapy monitoring. One relatively recent example of this is the combination of positron emission tomography (PET) and magnetic resonance (MR) systems into one integrated device. The first modality allows for obtaining quantitative information on function and metabolism *in vivo* by measuring the distribution of molecules (radiotracers) labelled with positron-emitting radionuclide. The second modality measures magnetic moments of ^{1}H to obtain anatomical and functional information, such as blood perfusion, blood flow velocities or diffusion. The combination of these two modalities has opened a range of new clinical applications and research opportunities, with current emphasis on brain [1–3] and cardiovascular [4] imaging. There is a growing number of these high-end devices (currently eight in the UK).

It is being increasingly recognized and demonstrated that information from complementary modalities, and from multiple time points, can be successfully combined to deliver image quality benefits compared to conventional independent processing. One particular feature of PET/MR is that the acquisitions can be carried out truly simultaneously, giving the opportunity to use information from both modalities to characterize motion, see [5,6] for reviews. Many methods exploit the simultaneity of MR and PET acquisitions, and the different properties of the two modalities for mutual benefit. MR generally provides superior structural contrast and better spatial and temporal resolution. Hence, advanced MR sequences combined with iterative reconstruction methods are often used to obtain images for motion estimation via registration. Such techniques allow time-resolved—or more often—gate-resolved (with a 'gate' corresponding to a motion state) images to be obtained, with recent advances for joint cardiac and respiratory motion estimation and correction [7,8]. However, the flexibility of MR means that often additional diagnostic acquisitions are required, precluding continuous MR motion acquisition, whereas PET data are available throughout the acquisition. Hence, other methods build motion models parametrized by surrogate signals derived from the PET or interlaced MR navigator data [9]. These models can be estimated on part of the data such that other MR sequences can be used while PET data can still be collected, allowing correction for quasi-periodic motion due to respiration [10] or head movement [11].

From a researcher perspective, implementing these methods or developing new methods is very challenging. Although PET/MR manufacturers provide tools for data manipulation and image reconstruction, these tools may not have all the desired capabilities and are generally not flexible to customization due to their proprietary nature. There is therefore strong interest in open source software (OSS) that can be used for some or all of the data processing.

Examples of MR or nuclear medicine image reconstruction OSS are given in table 1. However, none of these packages can reconstruct both PET and MR data, and although it would be possible

Table 1. Examples of established OSS for biomedical tomographic image reconstruction and the individually supported modalities.

software	modalities reconstructed
Gadgetron [12,13]	MRI
BART [14]	MRI
STIR [15]	PET and SPECT
NiftyPET [16]	PET
RTK [17]	CBCT, CT and in the future SPECT
CASToR [18]	PET, SPECT and some CT support
MIRT [19]	PET, CT, SPECT, MRI (simulated data)

to use independent reconstruction frameworks, the onus would then be on the user to deal with file types and orientation conventions, as well as potentially registration and resampling. Furthermore, a combined framework also allows for multiple image modalities to be optimized simultaneously for truly synergistic reconstructions, as well as the simultaneous estimation of motion fields.

We are therefore developing an OSS framework called the Synergistic Image Reconstruction Framework (SIRF) [20]. This development is led by the Collaborative Computational Platform on Synergistic Reconstruction for Biomedical Imaging CCP SyneRBI www.ccpsynerbi.ac.uk.

SIRF was developed for synergistic PET/MR image reconstruction, aiming to exploit the rich cross-modality information during the reconstruction of both the PET and MR images. SIRF provides researchers with an enabling platform to develop and test novel algorithms on PET/MR patient data, and aims to eliminate the significant technical challenges when interfacing with data from different vendors and proprietary software. SIRF integrates with another OSS called the Core Imaging Library (CIL) [21,22], which provides advanced optimization and regularization methods. In addition, SIRF has capabilities for image registration and motion management, as outlined in §2, that are crucial for multi-modality data. The Operator Discretisation Library (ODL) [23] is similar in concept to CIL + SIRF, in that it provides a framework for algorithm development relying on other OSS packages for actual computations. However, there is currently no support for complex data (needed for MR), nor registration.

This paper briefly describes additional functionality and the enhanced integration with CIL added to SIRF since the publication of a previous article on the software [20], and describes an application of this work in the context of respiratory motion correction for simultaneously acquired PET/MR. Firstly, the use of a regularized reconstruction of gated MR data is illustrated, allowing derivation of high quality motion fields, which can then be used for a motion-compensated image reconstruction (MCIR) of the MR data with the fast iterative shrinkage-thresholding algorithm (FISTA) to reduce motion artefacts. These motion fields are then used in an MCIR for the PET data together with a convex optimization algorithm, the primal-dual hybrid gradient (PDHG) algorithm.

2. Motion estimation and correction in SIRF

Many image reconstruction methods can be formulated as an optimization problem:

$$\hat{x} = \underset{x \in \mathbb{X}}{\arg\min}\, D(Ax, d) + g(x), \tag{2.1}$$

where $x \in \mathbb{X}$ is the discretized image (represented as a vector), $\hat{x}$ is the estimated optimal reconstruction, A is an operator modelling the system (in SIRF, the '`AcquisitionModel`'), d is the measured data (represented as a vector), D is the data fidelity function that measures data goodness-of-fit (often chosen as the negative of the log-likelihood for PET or the L2-norm for MR)

and g is a regularization function imposing desirable properties on the image. In many modalities, the acquisition model is an affine operator:

$$Ax = Kx + b, \tag{2.2}$$

with K the system matrix and b a background term. Details for MR and PET will be given below.

To be able to do motion correction, the data are split into several motion states, usually called 'gates', resulting in multiple vectors d_i. There are numerous techniques for performing motion correction. Two of the most common methods are the reconstruct-transform-add (RTA) scheme [24,25], in which correction is performed after reconstruction, and the MCIR scheme [26–31], in which the motion is incorporated into the acquisition model, one for each gate, resulting in the following equation:

$$\hat{x}_{\mathrm{MCIR}} = \arg\min_{x \in \mathbb{X}} \sum_{i=1}^{n} D(A_{\mathrm{MCIR}\,i}\, x, d_i) + g(x), \tag{2.3}$$

with n the number of gates and $A_{\mathrm{MCIR}\,i}$ the acquisition model for the i-th gate (see below) which includes motion information between the gate and a reference position. MCIR therefore finds a single image from all the gates.

Both of the RTA and MCIR schemes assume that the motion is known. One common way to determine the required motion information is to reconstruct motion resolved images (i.e. one for each gate) and then estimate the spatial transformation between the gates using image registration [24,32,33].

As mentioned in Ovtchinnikov *et al.* [20], registration and resampling in SIRF can be achieved by using the wrapped functionality provided by NiftyReg [34,35], including estimation of rigid, affine and non-rigid deformations (modelled via B-splines). This functionality allows the estimation of motion from reconstructed images of one modality, and then the application of the deformation fields on images from another modality. Since our previous publication, SIRF functionality has progressed further, with specific focus on enabling its use with motion estimation and correction. Some of these enhancements are described below.

(a) Adjoint resampling

In MCIR, the acquisition model for the motion-corrected image, $A_{\mathrm{MCIR}\,i}$, of a given gate, i, is often computed as a composition of the acquisition model for the image at gate i, $A_{\mathrm{acq}\,i}$, and a warp operator, W_i:

$$A_{\mathrm{MCIR}\,i} = A_{\mathrm{acq}\,i} \circ W_i, \tag{2.4}$$

where $\circ$ is the composition operator (see §2b). Here, W_i is a resampling operator that maps an image at the reference position to the image at gate i. The resampling uses interpolation (such as tri-linear or cubic splines) and is a linear operation in terms of the image values.

Many iterative reconstruction techniques rely on the gradient of the data fitting term in equation (2.1) with respect to x. Using the chain rule, this can be computed in terms of the gradient of the data fitting term without warping and the gradient of the warping operator. The latter is given by the adjoint operation W_i^*. The reader should note that this operation differs from the inverse, W_i^{-1}, which is used for the inverse transform in RTA and in many other registration applications. In the case of motion warping, the adjoint can be thought of as the switching of the interpolation types (from push to pull or vice versa) when reversing the motion.

The adjoint of the warp operator was implemented in SIRF according to McClelland *et al.* [36]. The resampling can handle images of different sizes, orientation and voxel size. For a given deformation field, a SIRF resampler object will perform the warp using the '`forward`' method and the adjoint warp using the '`backward`' method (in Python, aliased to '`direct`' and '`adjoint`', respectively, for CIL compatibility):

Adjoint resampling with SIRF

```
import sirf.Reg as reg
resampler = reg.NiftyResample()
resampler.set_reference_image(im_ref)
resampler.set_floating_image(im_flo)
resampler.add_transformation(transformation)
resampler.set_interpolation_type_to_linear()
adjoint_im = resampler.adjoint(im_ref)
```

Tests were implemented in SIRF and CIL to ensure that these operators W_i^* and $A^*_{\mathrm{MCIR}\,i}$ (without background term) were indeed the adjoint of their forward operators. For two linear operators A and A^* to be considered the adjoint of one another, the following equality must hold:

$$\langle Ax, y\rangle = \langle x, A^*y\rangle, \tag{2.5}$$

for all x and y, where $\langle .,. \rangle$ denotes the inner product in the respective space. In the case of motion warping, x and y are both images, but in the case of the acquisition model, x is in the reconstruction space (i.e. an image) and y is in the raw acquisition space (such as a sinogram for PET).

(b) Enhanced integration with CIL

CIL provides a general optimization framework for imaging applications [21,22]. Many of the provided algorithms solve the following problem:

$$\begin{aligned}\hat{x} &= \arg\min_{x\in\mathbb{X}} f(K(x)) + g(x),\\ &= \arg\min_{x\in\mathbb{X}} \sum_{i=1}^{n} f_i(K_i(x)) + g(x).\end{aligned} \tag{2.6}$$

The MCIR optimization problem equation (2.3) can then be implemented by taking f_i and K_i as the data fidelity and MCIR acquisition model for each gate i, respectively, and g as a regularization function. As previously discussed in §2a, for each motion gate of MCIR, one needs to compose the acquisition model with the warp operator. This can be achieved by leveraging the '`CompositionOperator`' from the CIL code base, an example of which is given below. The sum over gates can be written using the block framework scheme implemented in CIL:

MCIR problem

```
from cil.optimisation.operators \
    import CompositionOperator, BlockOperator
Ki_list = []
for i in range(n_gates):
    Ki_list.append(CompositionOperator(acq_models[i], resamplers[i]))

K = BlockOperator(*Ki_list)
```

where '`BlockOperator`' constructs an operator from a list that when applied to an input image, computes the output from each operator in the list and stores the results in a '`BlockDataContainer`'. Similar code can be used for the data fidelity term using '`BlockFunction`'. The user can then choose the algorithm to solve the optimization problem by taking into account the 'smoothness' characteristics of the objective function. With this

consideration, for the MR section of this paper FISTA was used, whereas PDHG was used for the PET component. For a detailed description of the CIL framework, please refer to [21,22].

(c) Registering and resampling complex images

Since MR images are reconstructed from complex data in the *k*-space domain, the resultant images are also complex. To be able to perform motion estimation and correction with MR images, it was therefore necessary for SIRF to be able to register and resample complex images. Registering MR images is relatively straightforward—in most cases, the anatomical information is best described by the absolute component of the image, and so SIRF was extended to use the absolute part by default. The ability to resample complex images did not previously exist in NiftyReg, and so this functionality was added to SIRF.

(d) Statistical Parametric Mapping

Lastly, the rigid registration functionality of the Statistical Parametric Mapping (SPM) [37] is now also available in SIRF. SPM is an OSS that has been designed for the analysis of brain imaging data sequences. Since it was created to process modalities of high temporal resolution, such as fMRI, it is capable of performing rigid registrations over many time points both quickly and to sub-voxel accuracy. Registration with SPM requires Matlab [38], which can be cumbersome if the rest of a workflow has been implemented in another language, such as Python. The wrapping mechanism employed by SIRF (described in greater detail in [20]) is advantageous in this regard; the underlying C++ SIRF code interfaces with the Matlab SPM code. This means that, as per the rest of the SIRF code base, the wrapped SPM functionality can be accessed from Matlab, C++ and Python. Furthermore, by changing just one line of code, the user is able to switch between NiftyReg and SPM registration routines:

Interchangeability of registration packages within SIRF

```
import sirf.Reg as reg
if use_niftyreg:
    algo = reg.NiftyAladinSym()
else:
    algo = reg.SPMRegistration()
algo.set_reference_image(im_ref)
algo.set_floating_image(im_flo)
algo.process()
TM = algo.get_transformation_matrix_forward()
```

3. Motion correction for cardiac PET/MR

In the following, we present an example of the above-described framework using an *in vivo* cardiac PET/MR scan. A non-Cartesian sampling scheme is presented, which allows for the estimation of respiratory motion. This motion information is then used in MCIR to improve simultaneously acquired MR and PET data.

The data used throughout this section consist of a 3:18 min PET/MR scan, which was carried out in a patient 182 min after an injection of 341 MBq of ^{18}F-FDG. The MR acquisition used here was a three-dimensional (3D), three-point Dixon scan (echo times: 1.2, 2.7 and 4.2 ms) with a field-of-view of $400 \times 400 \times 400\,\text{mm}^3$ and a spatial resolution of 1.9 mm along foot-head and $3.2 \times 3.2\,\text{mm}^2$ in the transversal plane. The readout was oriented along the head-foot direction and the number of acquired readout lines was such that the *k*-space was oversampled in the phase encoding plane by approximately a factor of 2. In the following, only the first echo was used.

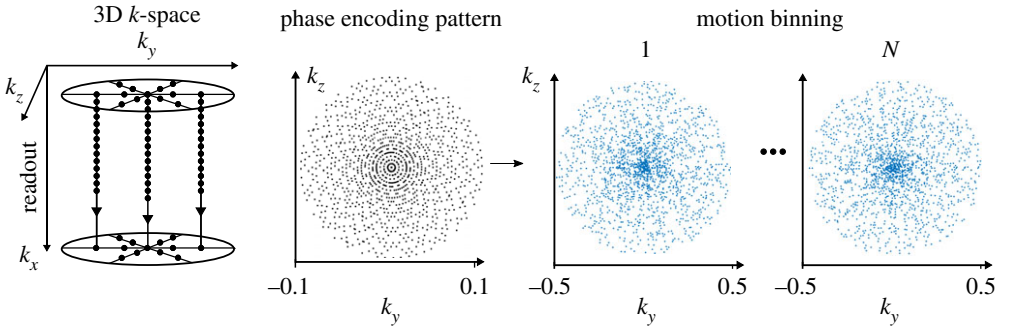

Figure 1. Golden radial phase encoding (GRPE). GRPE combines Cartesian sampling along k_x with radial sampling along k_y and k_z. The Golden radial sampling ensures that the k-space data are well distributed in the k_y–k_z phase encoding space even after splitting the data into N different motion gates (motion binning).

(a) Respiratory motion estimation and correction for cardiac magnetic resonance

In this section, a demonstration is given of the estimation of respiratory motion from a 3D non-Cartesian MR scan. The motion information is then used in an MCIR to improve the MR image quality. A new acquisition model was combined with the iterative reconstruction schemes available in CIL to ensure high image quality, even for highly undersampled data. 3D non-rigid motion fields are obtained using spline-based image registration and then applied during image reconstruction to minimize respiratory motion artefacts.

(i) Golden radial phase encoding

Non-Cartesian MR sampling schemes are of great interest for motion-estimation and motion-correction. Even if the data are separated retrospectively into different motion gates (e.g. different phases of the breathing cycle), the k-space data are still well distributed in k-space covering both high and low spatial frequencies. In addition, high image quality can be achieved even from very few acquired k-space points (i.e. high undersampling) using iterative image reconstruction schemes. The challenge of non-Cartesian trajectories is that the standard fast Fourier transform (FFT) cannot be applied directly to the data. The non-uniform fast Fourier transform (NUFFT) is required instead, to allow for the transformation of non-Cartesian k-space data to Cartesian image data. Here, as illustrated in figure 1, a golden radial phase encoding (GRPE) sampling scheme was used [39,40]. This is a 3D acquisition scheme in which frequency encoding (k_x) is carried out along parallel lines. Phase encoding points are obtained along a radial pattern in the two-dimensional phase-encoding plane k_y–k_z. All phase encoding points along a radial line are acquired and the angle between two successive GRPE lines is calculated based on the Golden angle of 111.24°. Figure 1 also shows two examples of the distribution of k-space points after separating it into different motion gates.

The acquisition model, A_{GRPE}, for this non-Cartesian trajectory implemented in SIRF is, therefore

$$A_{\mathrm{GRPE\,i}} = F_i C_c, \tag{3.1}$$

where C is the coil sensitivity map for each coil c and F is the Fourier transform which is used to transform the data of each gate i from image to k-space. For Cartesian sampling schemes, F can be realized by FFT followed by a sampling mask to select the data points for each gate. For the non-Cartesian GRPE, F consists of FFT along the k_x-direction before applying the NUFFT in the k_y–k_z plane. GRPE allows for the calculation of C from the data itself using the fully sampled k-space centre in the phase encoding plane. The implementations used to realize this acquisition model are wrapped in SIRF from Gadgetron [12,13].

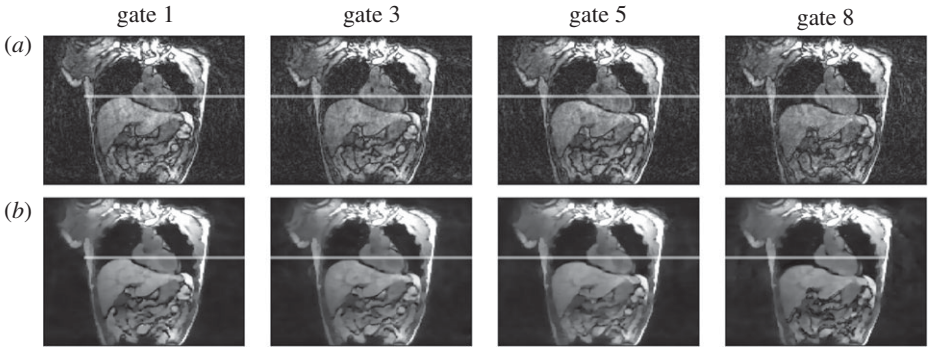

Figure 2. Respiratory-resolved gates reconstructed (row *a*) without and (row *b*) with TV regularization. Columns indicate various motion gates. The horizontal line represents the superior-most diaphragm position in the reference gate.

(ii) Reconstruction of respiratory gates

The *k*-space data were acquired during free-breathing. A self-navigator was extracted from the central k_x-line ($k_y = k_z = 0$). Data were separated into eight different respiratory gates based on the amplitude of the self-navigator [41,42]. A sliding window reconstruction with an overlap of 25% was used, leading to an undersampling factor of approximately three for each gate. Choosing the number of gates is a trade-off between emerging undersampling artefacts and a more accurate motion estimation. Previous studies have shown accurate respiratory motion correction of the liver (where the motion amplitudes exceed those expected in cardiac applications) with as few as five gates [43]. The gates were subsequently reconstructed using the implementation of FISTA [44] in CIL, without and with spatial total variation (TV) regularization [45]. We refer to [21] for more information on how to use FISTA via CIL. The MR optimization problem was mapped to equation (2.6) using

— $K_i = A_{\mathrm{GRPE}\ i}$, as described in §3a(i) and equation (2.4);
— the fidelity functions $f_i(x) = ||(K_i(x) - d_i)||^2$ as the least-squares function due to the Gaussian noise distribution for MR data, with d_i representing the data for the *i*-th respiratory gate; and
— g as the TV or total generalized variation (TGV) [46] regularization function.

Figure 2 shows four of these eight motion gates comparing both reconstruction algorithms. Changes in the anatomy during the breathing cycle are clearly visible. The TV regularization leads to suppression of undersampling artifacts and an improved depiction of the anatomy.

(iii) Estimation of respiratory motion fields

The respiratory gates were then used in a non-rigid image registration to estimate the 3D respiratory motion fields, i.e. for each voxel its changes during the respiratory cycle were estimated. This was done via the SIRF wrapper to the NiftyReg spline-based registration algorithm as described in §2.

End-expiration was selected as reference motion gate. Pairwise image registration was carried out to obtain the forward transformation from the reference gate to all other respiratory gates. An example of the estimated motion for a single gate is shown in figure 3, which is superposed on top of the reconstruction of that gate.

(iv) Motion-corrected MR image reconstruction

The MCIR optimization problem was constructed as in §2b and solved with FISTA. Figure 4 shows the final MCIR images reconstructed with FISTA without and with additional regularization.

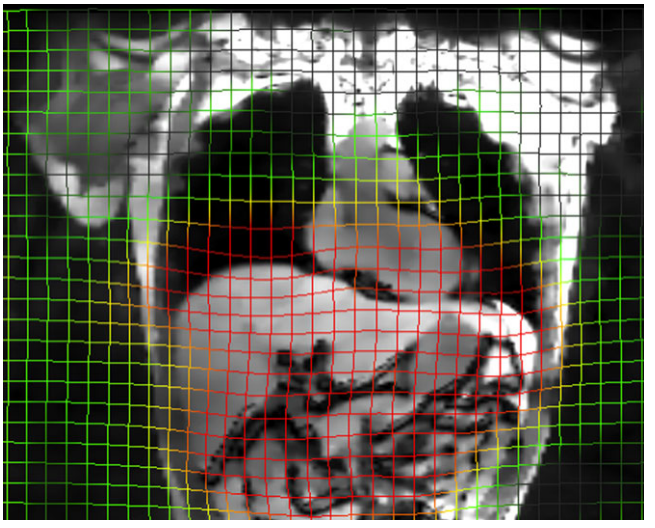

Figure 3. Motion fields estimated for a single gate, represented as a warped Cartesian grid, superposed on top of the corresponding reconstruction of that gate. For emphasis, full inspiration is shown as this has the largest motion compared to the reference state (end-expiration). Here, the colour gradient from green to red describes increasing displacement amplitude.

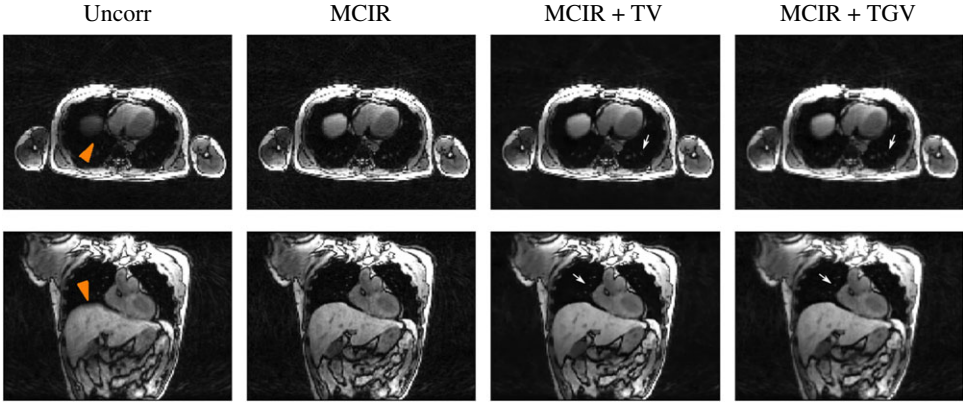

Figure 4. Uncorr: image reconstruction without motion correction with blurring due to respiratory motion clearly visible (orange arrow heads). MCIR: MCIR without regularization. MCIR + TV: MCIR with TV regularization. MCIR + TGV: MCIR with TGV regularization. Regularization leads to a suppression of undersampling artefacts while preserving even small image features such as lung vessels (white arrows).

Compared to the uncorrected reconstruction, the minimization of motion artefacts using MCIR is clearly visible. Further improvement in image quality due to the suppression of residual undersampling artefacts using TV and TGV regularization can also be seen.

(b) Incorporating estimated motion into positron emission tomography reconstruction

As PET/MR acquisitions are simultaneous, the motion fields from the previous section can be used to reconstruct a motion-corrected PET image. In practice, there can be a coordinate transformation between the PET and MR images, for instance due to gantry misalignment. This was estimated by performing a rigid registration between simultaneous MR and PET images,

where the PET image was reconstructed without attenuation correction (AC). The MR-derived deformation fields were then transformed into the PET coordinate system.

As mentioned above, the GRPE acquisition was carried out as a three-point Dixon scan. This allowed for the separation of fat and water tissue and the calculation of a segmentation-based AC map [47]. The AC map was obtained from the MCIR MR images to ensure it was also in the reference motion state. The construction of the MR-based AC map was not carried out in SIRF as it required segmentation tools not yet implemented in SIRF.

In PET, A_{acq} is given for gate i as

$$A_{\text{acq i}} = \beta_i S_i G + b_i, \tag{3.2}$$

where G is the geometric projector (e.g. produced via ray tracing); S_i is the acquisition sensitivity model; b_i is a background term obtained by summing an estimate for the accidental and scattered coincidences; and β_i is the relative time corresponding to gate i, so that $\sum_{\text{i}} \beta_{\text{i}} = 1$. S_i is, in turn, a product of detector and geometric sensitivity and attenuation factors. In the current experiment, the accidental and scatter estimates were computed from the ungated data and $b_i = \beta_i b$. The reader should note this is a simplified assumption that is only approximately valid under small deformations (validated for brain scans in [48]). In other contexts, independent scatter estimates may become necessary. Attenuation factors depend on the motion state. Therefore, for known motion, as is the case with MCIR, attenuation factors are computed by warping the AC maps into the correct position prior to starting the reconstruction, such that S_i is fixed for each gate. The implementations used to realize this acquisition model are wrapped in SIRF from the Software for Tomographic Image Reconstruction (STIR) [15].

The warped forward model $A_{\text{MCIR }i}$ is defined in equation (2.4) and (3.2). We model the data d_i corresponding to gate i as Poisson variables. As the Poisson log-likelihood can be written in terms of the Kullback–Leibler (KL) divergence (up to constant terms), the MCIR problem for PET corresponds to solving equation (2.3) with D as the KL divergence and $g = \|\nabla \cdot\|_{2,1}$ as the isotropic TV.

In order to reformulate the problem as an instance of the general framework in equation (2.6), let us define K_i as the linear part of $A_{\text{MCIR i}}$, that is to say $K_i = \beta_i S_i G \circ W_i$, and f_i, g as

$$f_i(y) = \text{KL}\left(d_i, y + b_i\right)$$

and

$$g(x) = \alpha \|\nabla x\|_{2,1}.$$

For a convex function f, the convex conjugate function is defined as $f^*(u) = \sup_x \langle u, x\rangle - f(x)$. The minimization problem equation (2.6) can be solved via the saddle-point problem:

$$\arg\min_x \sup_{(y_i)} \sum_{i=1}^{n} \langle K_i x, y_i\rangle - f_i^*(y_i) + g(x), \tag{3.3}$$

which introduces the dual variable $y = (y_1, \ldots y_n)$. In order to solve equation (3.3), we use the PDHG algorithm [49]. PDHG solves equation (3.3) by alternatively minimizing with respect to the primal variable x and maximizing with respect to the dual variable $y = (y_1, \ldots, y_n)$, which it achieves using the proximal operators of g and of f^*. While the proximal operator of the Kullback–Leibler divergence convex conjugate admits an explicit expression, this is not the case for the proximal operator of the TV regularizer, which is approximated with FISTA in inner iterations.

In order to observe the effect of motion correction, we compare the reconstructions obtained with the forward models $A_{\text{acq }i}$ and $A_{\text{MCIR i}} = A_{\text{acq }i} \circ W_i$. The reconstructions were performed under identical algorithms schemes (PDHG with the same number of iterations, amount of regularization and step-size parameters). The results are shown in figure 5. The effect of respiratory motion correction is that the cardiac structures are sharper, particularly at the level of the papillary muscles. However, these results are preliminary and need further optimization of regularization and optimizer settings. For example, we found that the number of iterations

Figure 5. Comparison of TV-regularized PDHG reconstructions with (top) and without (bottom) motion correction for the axial (left), sagittal (centre) and coronal (right) views. Both PET reconstructions were run for 1000 iterations with regularization strength of $\alpha = 3$. In the motion corrected case, a sharpening of the papillary muscles can be seen.

required to obtain images of good visual quality was higher in the MCIR context than without gating. This will be studied in future work.

4. Conclusion and outlook

In this paper, we have presented recent improvements of SIRF regarding PET/MR, concentrating on motion correction and in particular MCIR. We have shown how respiratory gates can be reconstructed from a non-Cartesian 3D MR scan and how non-rigid respiratory motion fields can be obtained using the NiftyReg integration in SIRF. These motion fields can then be used for MCIR of both MR and PET. The integration of CIL with SIRF allowed for the use of regularized FISTA and PDHG optimization schemes.

The modular nature of SIRF and CIL enables rapid prototyping of algorithms. We have demonstrated how MCIR can be implemented in a scheme that is very similar across different imaging modalities. This allows ideas from different communities of imaging and inverse-problem scientists to be conveniently shared. Furthermore, we showed how the consistent interface between SIRF and CIL allows individual components, including regularizers and optimizers, to be interchanged and compared while keeping the remaining components static. This enables researchers to optimize methods for their application.

While we have only used spatial regularization for the reconstruction of the respiratory gates, the application of additional regularization along the motion dimension should further improve image quality and hence motion accuracy [50,51].

The simultaneous data acquisition and the motion correction using the same motion transformation for PET and MR ensures their optimal spatial alignment. Therefore, the information of one modality could also be applied as guided regularization for MCIR of the other modality to further improve image quality [52–55], and ultimately joint (or 'synergistic') reconstruction [56–59].

In this paper, motion estimation has been carried out as a separate step to MCIR and requires the reconstruction of motion-resolved gates. Although TV regularization ensured high image quality even for high undersampling factors of the GRPE MR data, this approach still requires that sufficient data are available in each gate to allow an accurate motion estimation. In addition, the information about respiratory motion available from PET was not used at all for motion

estimation. Registration of multi-modal data has been shown to be beneficial when correcting for both respiratory motion and cardiac contraction [7]. Combining MCIR and motion estimation into a single optimization would overcome these limitations. By carrying out the reconstruction of a motion-corrected MR and PET image while also optimizing the joint motion fields would provide the optimal synergistic use of the simultaneous PET/MR acquisition [26,60–65]. To achieve this, the calculation of gradients with respect to the motion field parameters (e.g. spline weights for the spline-based motion fields used in NiftyReg) is required and will be part of future work on SIRF.

While the use of OSS for prototyping of reconstruction algorithms provides many benefits, there are also limitations to SIRF when compared with vendor's proprietary software. Vendors have often highly optimized their particular algorithms for their system. When using SIRF, the user will need to determine appropriate parameters and hyperparameters, e.g. for regularization strengths but also for physical properties like system resolution if performing resolution modelling. Similarly, the engines used by SIRF have been optimized for research exploration rather than performance. Hence, computation time when using SIRF is longer than when using vendor software.

There is increasing interest in integrating deep learning (DL) into PET reconstruction [66]. Common DL frameworks include PyTorch [67] and Tensorflow [68] in Python, as well as Matlab's deep learning toolbox [69]. Furthermore, the use DL for image registration is a field that is rapidly expanding [70,71], and which can be leveraged by SIRF. These frameworks can all be used in conjunction with SIRF to implement and explore state-of-the-art methods.

New multi-modality systems are now available or under development, for instance SPECT/MR [72] and (non-simultaneous) SPECT/PET/CT such as the recent Mediso AnyScan clinical system and pre-clinical Bruker Albira Si, enabling opportunities for multi-radiotracer studies. At the same time, top-of-the-range multi-modality systems are expensive and combining single-modality scans from different time-points and systems can provide more cost-effective solutions and faster worldwide adaptation, which again demands the ongoing developments in spatial alignment. While imaging research and software methods are both developing rapidly, the challenging opportunity for cross-modality synergistic methods remains open. We intend to continue to develop SIRF for researchers to be able to exploit synergy in multi-modal, multi-contrast, multi-time point information for a greater range of applications.

Ethics. Patients gave written, informed consent to take part in the study and to undergo a PET/MR scan after the original PET/CT scan without any additional injection of a radionuclide tracer. The study was approved by National Research Ethics Service Committee at King's College London (no. 15/LO/0978).

Data accessibility. Reconstruction scripts and installation instructions for the specific versions of code used in this research can be found in our contributor's GitHub page. This resource includes information of supported python versions and CI/CD testing.

Authors' contributions. R.B. developed PET and registration functionality, co-developed the PET MCIR reconstruction script, ran PET experiments and drafted part of the manuscript. E.Pas. developed the interoperability between SIRF and CIL, co-developed the PET and MR MCIR reconstruction scripts and ran the PET reconstructions on the STFC cluster. E.Pap. co-developed the PET MCIR reconstruction script. C.K. and J.M. developed the GRPE acquisition model, the MR MCIR reconstruction script, carried out the MR reconstruction and drafted this part of the manuscript. R.N. helped with the development of used MR sequences with CK. C.D. co-developed the PET MCIR reconstruction script, carried out PET experiments and drafted this part of the manuscript. JRM and B.E. implemented adjoint image resampling functionality. E.O. developed the core of the SIRF code base. C.d.C.L. aided with code infrastructure, example scripts, testing and continuous integration. A.G. developed code for handling patient orientation as well as aiding draft the PET and motion correction sections of the paper. M.J.E. aided with mathematical theory behind PDHG. K.T. provided general oversight of the project and software and drafted part of the manuscript. All authors read and approved the manuscript.

Competing interests. Dr Neji is an employee of Siemens Healthcare.

Funding. This work was funded by the UK EPSRC grants 'Computational Collaborative Project in Synergistic PET/MR Reconstruction' (CCP PETMR) EP/M022587/1 and its associated Software Flagship project EP/P022200/1; the 'Computational Collaborative Project in Synergistic Reconstruction for Biomedical

Imaging' (CCP SyneRBI) EP/T026693/1; 'A Reconstruction Toolkit for Multichannel CT' EP/P02226X/1 and 'Collaborative Computational Project in tomographic imaging' (CCPi) EP/M022498/1 and EP/T026677/1; 'PET++: Improving Localization, Diagnosis and Quantification in Clinical and Medical PET Imaging with Randomized Optimization' EP/S026045/1. This work made use of computational support by CoSeC, the Computational Science Centre for Research Communities, through CCP SyneRBI and CCPi.

Acknowledgements. We thank Simon Arridge, David Atkinson, Julian Matthews, Andrew Reader, Steven Sourbron, Charalampos Tsoumpas and Martyn Winn for co-organizing the CCP PETMR/SyneRBI network, its community for feedback, and Jakob S. Jørgensen and other members of CCPi for interactions on the software and algorithms. Computing resources were provided by STFC Scientific Computing Department's SCARF cluster and the STFC Cloud.

References

1. Zhang XY, Yang ZL, Lu GM, Yang GF, Zhang LJ. 2017 PET/MR imaging: new frontier in Alzheimer's disease and other dementias. *Front. Mol. Neurosci.* **10**, 343. (doi:10.3389/fnmol.2017.00343)
2. Barthel H, Sabri O. 2018 Neurodegeneration imaging. In *PET/MR imaging: current and emerging applications* (eds L Umutlu, K Herrmann), pp. 99–106. Basel, Switzerland: Springer International Publishing.
3. Chen Z, Jamadar SD, Li S, Sforazzini F, Baran J, Ferris N, Shah NJ, Egan GF. 2018 From simultaneous to synergistic MR-PET brain imaging: a review of hybrid MR-PET imaging methodologies. *Hum. Brain Mapp.* **39**, 5126–5144. (doi:10.1002/hbm.24314)
4. Robson PM, Dey D, Newby DE, Berman D, Li D, Fayad ZA, Dweck MR. 2017 MR/PET imaging of the cardiovascular system. *JACC: Cardiovascul. Imag.* **10**, 1165–1179. (doi:10.1016/j.jcmg.2017.07.008)
5. Gillman A, Smith J, Thomas P, Rose S, Dowson N. 2017 PET motion correction in context of integrated PET/MR: current techniques, limitations, and future projections. *Med. Phys.* **44**, e430–e445. (doi:10.1002/mp.12577)
6. Munoz C, Kolbitsch C, Reader AJ, Marsden P, Schaeffter T, Prieto C. 2016 MR-based cardiac and respiratory motion-compensation techniques for PET-MR imaging. *PET Clin.* **11**, 179–191. (doi:10.1016/j.cpet.2015.09.004)
7. Kolbitsch C, Neji R, Fenchel M, Schuh A, Mallia A, Marsden P, Schaeffter T. 2018 Joint cardiac and respiratory motion estimation for motion-corrected cardiac PET-MR. *Phy. Med. Biol.* **64**, 015007. (doi:10.1088/1361-6560/aaf246)
8. Munoz C, Neji R, Kunze KP, Nekolla SG, Botnar RM, Prieto C. 2019 Respiratory-and cardiac motion-corrected simultaneous whole-heart PET and dual phase coronary MR angiography. *Magn. Reson. Med.* **81**, 1671–1684. (doi:10.1002/mrm.27517)
9. McClelland JR, Hawkes DJ, Schaeffter T, King AP. 2013 Respiratory motion models: a review. *Med. Image Anal.* **17**, 19–42. (doi:10.1016/j.media.2012.09.005)
10. Manber R, Thielemans K, Hutton BF, Wan S, McClelland J, Barnes A, Arridge S, Ourselin S, Atkinson D. 2016 Joint PET-MR respiratory motion models for clinical PET motion correction. *Phys. Med. Biol.* **61**, 6515–6530. (doi:10.1088/0031-9155/61/17/6515)
11. Gillman AG, Rashidnasab A, Brown R, Dowson N, Thomas B, Fraioli F, Rose S, Thielemans K. 2019 PCA regression for continuous estimation of head pose in PET/MR. In *2019 IEEE Nuclear Science Symp. and Medical Imaging Conf. (NSS/MIC)*, pp. 1–3. (doi:10.1109/NSS/MIC42101.2019.9059846)
12. Hansen MS, Sørensen TS. 2013 Gadgetron: an open source framework for medical image reconstruction. *Magn. Reson. Med.* **69**, 1768–1776. (doi:10.1002/mrm.24389)
13. Gadgetron. 2020 Available at https://github.com/gadgetron.
14. Uecker M, Rosenzweig S, Holme HCM, Blumenthal M, Tan Z, Wang X, Tamir JI, Lustig M. 2020 mrirecon/bart: version 0.6.00. https://zenodo.org/record/3934312#.X7v4LOlxeHs.
15. Thielemans K, Tsoumpas C, Mustafovic S, Beisel T, Aguiar P, Dikaios N, Jacobson MW. 2012 STIR: software for tomographic image reconstruction release 2. *Phys. Med. Biol.* **57**, 867–883. (doi:10.1088/0031-9155/57/4/867)
16. Markiewicz PJ *et al.* 2018 NiftyPET: a high-throughput software platform for high quantitative accuracy and precision PET imaging and analysis. *Neuroinformatics* **16**, 95–115. (doi:10.1007/s12021-017-9352-y)

17. Rit S, Oliva MV, Brousmiche S, Labarbe R, Sarrut D, Sharp GC. 2014 The reconstruction toolkit (RTK), an open-source cone-beam CT reconstruction toolkit based on the Insight Toolkit (ITK). In *Journal of Physics: Conf. Series 2014 Mar 24*, vol. 489, p. 012079. IOP Publishing. (doi:10.1088/1742-6596/489/1/012079)
18. Merlin T, Stute S, Benoit D, Bert J, Carlier T, Comtat C, Filipovic M, Lamare F, Visvikis D. 2018 CASToR: a generic data organization and processing code framework for multi-modal and multi-dimensional tomographic reconstruction. *Phys. Med. Biol.* **63**, 185005. (doi:10.1088/1361-6560/aadac1)
19. Fessler JA. 2018 Michigan Image Reconstruction Toolbox. https://github.com/JeffFessler/MIRT.jl.
20. Ovtchinnikov E *et al.* 2020 SIRF: synergistic image reconstruction framework. *Comput. Phys. Commun.* **249**, 107087. (doi:10.1016/j.cpc.2019.107087)
21. Jørgensen JS *et al.* 2021 Core Imaging Library part I: a versatile Python framework for tomographic imaging. *Phil. Trans. R. Soc. A* **379**, 20200192. (doi:10.1098/rsta.2020.0192)
22. Papoutsellis E *et al.* 2021 Core Imaging Library - Part II: multichannel reconstruction for dynamic and spectral tomography. *Phil. Trans. R. Soc. A* **379**, 20200193. (doi:10.1098/rsta.2020.0193)
23. Adler J *et al.* 2018 Operator discretisation library ODL. https://zenodo.org/record/1442734#.X7-Z5ulxeHs.
24. Klein GJ, Reutter BW, Huesman RH. 1996 Non-rigid summing of gated PET via optical flow. In *Nuclear Science Symp., 1996. Conf. Record., 1996*, vol. 2, pp. 1339–1342. IEEE. (doi:10.1109/23.632704)
25. Picard Y, Thompson CJ. 1997 Motion correction of PET images using multiple acquisition frames. *IEEE Trans. Med. Imaging* **16**, 137–144. (doi:10.1109/42.563659)
26. Jacobson MW, Fessler JA. 2003 Joint estimation of image and deformation parameters in motion-corrected PET. In *2003 IEEE Nuclear Science Symp. Conference Record*, pp. 3290–3294. IEEE. (doi:10.1109/NSSMIC.2003.1352599)
27. Manjeshwar RM, Tao X, Asma E, Thielemans K. 2006 Motion compensated image reconstruction of respiratory gated PET/CT. In *3rd IEEE Int. Symp. on Biomedical Imaging: Macro to Nano, 2006*, pp. 674–677. Piscataway, NJ: IEEE. (doi:10.1109/ISBI.2006.1625006)
28. Qiao F, Pan T, Clark JW, Mawlawi OR. 2006 A motion-incorporated reconstruction method for gated PET studies. *Phys. Med. Biol.* **51**, 3769–3783. (doi:10.1088/0031-9155/51/15/012)
29. Batchelor PG, Atkinson D, Irarrazaval P, Hill DLG, Hajnal J, Larkman D. 2005 Matrix description of general motion correction applied to multishot images. *Magn. Reson. Med.* **54**, 1273–1280. (doi:10.1002/mrm.20656)
30. Manber R, Atkinson D, Thielemans K, Hutton B, Barnes A, O'Meara C, Wan S, Ourselin S, Arridge S. 2015 Practical PET respiratory motion correction in clinical simultaneous PET/MR. In *2015 IEEE 12th Int. Symp. on Biomedical Imaging (ISBI 2015)*, pp. 1580–1583. Piscataway, NJ: IEEE. (doi:10.1109/ISBI.2015.7164181).
31. Polycarpou I, Tsoumpas C, King AP, Marsden PK. 2015 Quantitative evaluation of PET respiratory motion correction using MR derived simulated data. *IEEE Trans. Nucl. Sci.* **62**, 3110–3116. (doi:10.1109/TNS.2015.2494593)
32. Lamare F, Cresson T, Savean J, Cheze Le Rest C, Reader AJ, Visvikis D. 2006 Respiratory motion correction for PET oncology applications using affine transformation of list mode data. *Phys. Med. Biol.* **52**, 121–140. (doi:10.1088/0031-9155/52/1/009)
33. Dey J, King MA. 2010 Non-rigid full torso respiratory motion correction of SPECT studies. In *Nuclear Science Symp. Conf. Record (NSS/MIC), 2010 IEEE*, pp. 2356–2358. Piscataway, NJ: IEEE. (doi:10.1088/0031-9155/52/1/009).
34. Modat M, Ridgway GR, Taylor ZA, Lehmann M, Barnes J, Hawkes DJ, Fox NC, Ourselin S. 2010 Fast free-form deformation using graphics processing units. *Comput. Methods Programs Biomed.* **98**, 278–284. (doi:10.1016/j.cmpb.2009.09.002)
35. Modat M, Cash DM, Daga P, Winston GP, Duncan JS, Ourselin S. 2014 Global image registration using a symmetric block-matching approach. *J. Med. Imag.* **1**, 024003. (doi:10.1117/1.JMI.1.2.024003)
36. McClelland JR *et al.* 2017 A generalized framework unifying image registration and respiratory motion models and incorporating image reconstruction, for partial image data or full images. *Phys. Med. Biol.* **62**, 4273. (doi:10.1088/1361-6560/aa6070)

37. Ashburner J, Barnes G, Chen Cc, Daunizeau J, Moran R, Henson R, Glauche V, Phillips C. 2013 *SPM8 Manual*. The FIL Methods Group (and honorary members). London, UK: Functional Imaging Laboratory.
38. MATLAB. 2020 *Release R2020a*. Natick, Massachusetts: The MathWorks Inc.
39. Boubertakh R *et al.* 2009 Whole-heart imaging using undersampled radial phase encoding (RPE) and iterative sensitivity encoding (SENSE) reconstruction. *Magn. Reson. Med.* **62**, 1331–1337. (doi:10.1002/mrm.22102)
40. Prieto C, Uribe S, Razavi R, Atkinson D, Schaeffter T. 2010 3D undersampled golden-radial phase encoding for DCE-MRA using inherently regularized iterative SENSE. *Magn. Reson. Med.* **64**, 514–526. (doi:10.1002/mrm.22446)
41. Buerger C, Prieto C, Schaeffter T. 2013 Highly efficient 3D motion-compensated abdomen MRI from undersampled Golden-RPE acquisitions. *Magma: Magn. Reson. Mater. Phys. Biol. Med.* **26**, 419–429. (doi:10.1007/s10334-013-0370-y)
42. Kolbitsch C, Neji R, Fenchel M, Mallia A, Marsden P, Schaeffter T. 2018 Respiratory-resolved MR-based attenuation correction for motion-compensated cardiac PET-MR. *Phys. Med. Biol.* **63**, 135008. (doi:10.1088/1361-6560/aaca15)
43. Grimm R *et al.* 2015 Self-gated MRI motion modeling for respiratory motion compensation in integrated PET/MRI. *Med. Image Anal.* **19**, 110–120. (doi:10.1016/j.media.2014.08.003)
44. Beck A, Teboulle M. 2009 Fast gradient-based algorithms for constrained total variation image denoising and deblurring problems. *IEEE Trans. Image Process.* **18**, 2419–2434. (doi:10.1109/TIP.2009.2028250)
45. Rudin LI, Osher S, Fatemi E. 1992 Nonlinear total variation based noise removal algorithms. *Physica D* **60**, 259–268. (doi:10.1016/0167-2789(92)90242-F)
46. Bredies K, Kunisch K, Pock T. 2010 Total generalized variation. *SIAM J. Imag. Sci.* **3**, 492–526. (doi:10.1137/090769521)
47. Martinez-Möller A, Souvatzoglou M, Delso G, Bundschuh RA, Chefd'hotel C, Ziegler SI, Navab N, Schwaiger M, Nekolla SG. 2009 Tissue classification as a potential approach for attenuation correction in whole-body PET/MRI: evaluation with PET/CT data. *J. Nucl. Med.* **50**, 520–526. (doi:10.2967/jnumed.108.054726)
48. Burgos N *et al.* 2014 Effect of scatter correction when comparing attenuation maps: application to brain PET/MR. In *2014 IEEE Nuclear Science Symp. and Medical Imaging Conf. (NSS/MIC)*, pp. 1–5, Piscataway, NJ: IEEE. (doi:10.1109/NSSMIC.2014.7430775).
49. Chambolle A, Pock T. 2011 A first-order primal-dual algorithm for convex problems with applications to imaging. *J. Math. Imag. Vision* **40**, 120–145. (doi:10.1007/s10851-010-0251-1)
50. Otazo R, Candès E, Sodickson DK. 2015 Low-rank plus sparse matrix decomposition for accelerated dynamic MRI with separation of background and dynamic components. *Magn. Reson. Med.* **73**, 1125–1136. (doi:10.1002/mrm.25240)
51. Cruz G, Atkinson D, Buerger C, Schaeffter T, Prieto C. 2016 Accelerated motion corrected three-dimensional abdominal MRI using total variation regularized SENSE reconstruction. *Magn. Reson. Med.* **75**, 1484–1498. (doi:10.1002/mrm.25708)
52. Bowsher JE, Johnson VE, Turkington TG, Jaszczak RJ, Floyd CE, Coleman RE. 1996 Bayesian reconstruction and use of anatomical a priori information for emission tomography. *IEEE Trans. Med. Imaging* **15**, 673–686. (doi:10.1109/42.538945)
53. Lu L, Ma J, Feng Q, Chen W, Rahmim A. 2015 Anatomy-guided brain PET imaging incorporating a joint prior model. *Phys. Med. Biol.* **60**, 2145–2166. (doi:10.1088/0031-9155/60/6/2145)
54. Ehrhardt MJ *et al.* 2016 PET reconstruction with an anatomical MRI prior using parallel level sets. *IEEE Trans. Med. Imaging* **35**, 2189–2199. (doi:10.1109/TMI.2016.2549601)
55. Schramm G, Holler M, Rezaei A, Vunckx K, Knoll F, Bredies K, Boada F, Nuyts J. 2017 Evaluation of parallel level sets and Bowsher's method as segmentation-free anatomical priors for time-of-flight PET reconstruction. *IEEE Trans. Med. Imaging* **37**, 590–603. (doi:10.1109/TMI.2017.2767940)
56. Ehrhardt MJ, Thielemans K, Pizarro L, Atkinson D, Ourselin S, Hutton BF, Arridge SR. 2015 Joint reconstruction of PET-MRI by exploiting structural similarity. *Inverse Prob.* **31**, 015001. (doi:10.1088/0266-5611/31/1/015001)

57. Knoll F, Holler M, Koesters T, Otazo R, Bredies K, Sodickson DK. 2017 Joint MR-PET reconstruction using a multi-channel image regularizer. *IEEE Trans. Med. Imaging* **36**, 1–16. (doi:10.1109/TMI.2016.2564989)
58. Mehranian A, Belzunce MA, McGinnity CJ, Bustin A, Prieto C, Hammers A, Reader AJ. 2019 Multi-modal synergistic PET and MR reconstruction using mutually weighted quadratic priors. *Magn. Reson. Med.* **81**, 2120–2134. (doi:10.1002/mrm.27521)
59. Arridge SR, Burger M, Ehrhardt MJ. 2020 Preface to special issue on joint reconstruction and multi-modality/multi-spectral imaging. *Inverse Prob.* **36**, 020302. (doi:10.1088/1361-6420/ab4abb)
60. Jacobson MW, Fessler J. 2006 Joint estimation of respiratory motion and activity in 4D PET using CT side information. In *3rd IEEE Int. Symp. on Biomedical Imaging: Macro to Nano, 2006*, pp. 275–278. Piscataway, NJ: IEEE. (doi:10.1109/ISBI.2006.1624906).
61. Prieto C, Batchelor PG, Hill DLG, Hajnal JV, Guarini M, Irarrazaval P. 2007 Reconstruction of undersampled dynamic images by modeling the motion of object elements. *Magn. Reson. Imaging* **57**, 939–949. (doi:10.1002/mrm.21222)
62. Fayad H, Odille F, Schmidt H, Würslin C, Küstner T, Felblinger J, Visvikis D. 2015 The use of a generalized reconstruction by inversion of coupled systems (GRICS) approach for generic respiratory motion correction in PET/MR imaging. *Phys. Med. Biol.* **60**, 2529–2546. (doi:10.1088/0031-9155/60/6/2529)
63. Bousse A, Bertolli O, Atkinson D, Arridge S, Ourselin S, Hutton BF, Thielemans K. 2015 Maximum-likelihood joint image reconstruction/motion estimation in attenuation-corrected respiratory gated PET/CT using a single attenuation map. *IEEE Trans. Med. Imaging* **35**, 217–228. (doi:10.1109/TMI.2015.2464156)
64. Odille F, Vuissoz PA, Marie PY, Felblinger J. 2008 Generalized reconstruction by inversion of coupled systems (GRICS) applied to free-breathing MRI. *Magn. Reson. Med.* **60**, 146–157. (doi:10.1002/mrm.21623)
65. Weller DS, Wang L, Mugler JP, Meyer CH. 2019 Motion-compensated reconstruction of magnetic resonance images from undersampled data. *Magn. Reson. Imaging* **55**, 36–45. (doi:10.1016/j.mri.2018.09.008)
66. Reader AJ, Corda G, Mehranian A, Ellis S, Schnabel JA. 2020 Deep learning for PET image reconstruction. *IEEE Trans. Rad. Plasma Med. Sci.* **5**, 1–25. (doi:10.1109/trpms.2020.3014786)
67. Paszke A *et al.* 2019 PyTorch: an imperative style, high-performance deep learning library. In *Advances in Neural Information Processing Systems 32* (eds H Wallach, H Larochelle, A Beygelzimer, F d'Alché-Buc, E Fox, R Garnett), pp. 8024–8035. Red Hook, NY: Curran Associates, Inc. https://arxiv.org/abs/1912.01703.
68. Abadi M *et al.* 2015 TensorFlow: large-scale machine learning on heterogeneous systems. http://arxiv.org/abs/1603.04467.
69. The MathWorks Inc. 2019 *Deep learning toolbox*. Natick, MA: MathWorks.
70. Balakrishnan G, Zhao A, Sabuncu MR, Guttag J, Dalca AV. 2018 An unsupervised learning model for deformable medical image registration. In *Proc. of the IEEE Conf. on Computer Vision and Pattern Recognition (CVPR)*. Piscataway, NJ: IEEE. (doi:10.1007/978-3-030-59716-0_19).
71. Heinrich MP, Hansen L. 2020 Highly accurate and memory efficient unsupervised learning-based discrete CT registration using 2.5D displacement search. In *Medical Image Computing and Computer Assisted Intervention – MICCAI 2020* (eds AL Martel, P Abolmaesumi, D Stoyanov, D Mateus, MA Zuluaga, SK Zhou, D Racoceanu, L Joskowicz), pp. 190–200. Cham, Switzerland: Springer International Publishing. (doi:10.1007/978-3-030-59716-0_19)
72. Hutton BF *et al.* 2018 Development of clinical simultaneous SPECT/MRI. *Br. J. Radiol.* **91**, 20160690. (doi:10.1259/bjr.20160690)